

Extreme black hole spin–orbit misalignment in x-ray binary MAXI J1820+070

Juri Poutanen^{1,2,3*}, Alexandra Veledina^{1,2,3}, Andrei V. Berdyugin¹,
Svetlana V. Berdyugina⁴, Helen Jermak⁵, Peter G. Jonker^{6,7}, Jari J. E. Kajava^{1,8},
Ilia A. Kosenkov¹, Vadim Kravtsov¹, Vilppu Piirola¹, Manisha Shrestha^{5,9},
Manuel A. P. Torres^{10,11}, Sergey S. Tsygankov^{1,2}

- 1: Department of Physics and Astronomy, FI-20014 University of Turku, Finland
 2: Space Research Institute of the Russian Academy of Sciences, Profsoyuznaya Str. 84/32, 117997 Moscow, Russia
 3: Nordita, KTH Royal Institute of Technology and Stockholm University, SE-10691 Stockholm, Sweden
 4: Leibniz-Institut für Sonnenphysik, Schöneckstr. 6, 79104 Freiburg, Germany
 5: Astrophysics Research Institute, Liverpool John Moores University, IC2, Liverpool Science Park, Brownlow Hill, L3 5RF, United Kingdom
 6: Department of Astrophysics/IMAPP, Radboud University, P.O. Box 9010, 6500 GL Nijmegen, The Netherlands
 7: SRON, Netherlands Institute for Space Research, Sorbonnelaan 2, NL-3584 CA Utrecht, The Netherlands
 8: Centro de Astrobiología - Departamento de Astrofísica (CSIC-INTA), Camino Bajo del Castillo s/n, S-28692 Villanueva de la Cañada, Spain
 9: Department of Physics & Astronomy, University of Denver, 2112 E Wesley Ave., 80208, Denver, USA
 10: Instituto de Astrofísica de Canarias, E-38205 La Laguna, Tenerife, Spain
 11: Departamento de Astrofísica, Universidad de La Laguna, E-38206 La Laguna, Tenerife, Spain

*Corresponding author. E-mail: juri.poutanen@utu.fi.

The observational appearance of black holes in x-ray binary systems depends on their masses, spins, accretion rate and the misalignment angle between the black hole spin and the orbital angular momentum. We used high-precision optical polarimetric observations to constrain the position angle of the orbital axis of the black hole x-ray binary MAXI J1820+070. Together with previously obtained orientation of the relativistic jet and the inclination of the orbit this allowed us to determine a lower limit of 40 degrees on the misalignment angle. Such a large misalignment challenges the models of quasi-periodic oscillations

observed in black hole x-ray binaries, puts strong constraints on the black hole formation mechanisms, and has to be accounted for when measuring black hole masses and spins from the x-ray data.

Astrophysical black holes are described by only two parameters: mass and spin. When a black hole resides in a binary system, there are additional parameters that define its observational appearance: the mass accretion rate and the misalignment angle between the black hole spin and the orbital spin. The standard methods to measure the black hole spin from the iron line spectroscopy (1) or the shape of the accretion disk spectrum (2) assume that the misalignment angle is small. On the other hand, the leading model for the low-frequency quasi-periodic oscillations observed in black hole x-ray binaries in the x-rays and optical, the Lense-Thirring solid-body precession of the hot flow around black hole (3–5), is based on the assumption that the misalignment is significant. Significant misalignment is also expected in x-ray binaries which have potentially high kick velocities acquired during formation (6). The large degree of misalignment puts strong constraints on the supernova explosion and black hole formation mechanisms, as it can only decrease during the accretion stage (7). Detection of orbital precession by LIGO/Virgo in the gravitational wave signals from a fraction of merging black holes (8) also argues in favor of non-zero misalignment in these systems (9).

In order to measure the misalignment angle in x-ray binaries one needs to determine 3D orientation of the black hole spin and the orbital axis. Jets are fueled and guided by the black hole spin (10), hence they can serve as a probe for the spin orientation. The jet inclination can be directly obtained in some cases when superluminal motions of ejected blobs are detected in radio (11). Together with the jet position angle measured using radio- or x-ray imaging, the black hole spin orientation can be determined. The orbital inclination can be obtained using optical photometric orbital variations and constraints coming from presence or absence of x-ray and disk eclipses (12, 13).

The black hole x-ray binary MAXI J1820+070 was discovered by the Monitor of All-sky X-ray Image on board the International Space Station on 2018 March 11 (14), and has been associated with the optical transient ASASSN-18ey (15, 16). Discrete relativistic ejections have been observed in the source both in radio and x-rays, which determined the jet inclination to the line-of-sight to be $i_{\text{jet}} = 63^\circ \pm 3^\circ$ and the position angle $\theta_{\text{jet}} = 25.1 \pm 1.4$ (17–19). Both of these have been found to be stable (in terms of orientation) over the entire duration of such ejections. After the end of the primary outburst, when the source decayed to quiescence, the orbital inclination was found to be within the range $66^\circ < i_{\text{orb}} < 81^\circ$ (13). To determine the 3D orientation of the orbital axis, one parameter was missing: its position angle θ_{orb} on the plane of the sky.

We monitored MAXI J1820+070 in *BVR* bands using high-precision optical polarimeters DIPol-2 (20) and DIPol-UF (21) during the whole outburst and in quiescence. The intrinsic polarization of the source was obtained by subtracting the contribution from the interstellar polarization measured using nearby field stars. In the outburst, when the relativistic jet was detected at the radio frequencies, the intrinsic polarization degree (PD) was about 0.5% and the

polarization angle (PA) was close to the jet position angle of about 25° (22, 23) measured from north via east. After the source faded in the x-rays, the observed PD had increased by a factor of 5–10 and the PA changed by 45° to about -20° (table S1 and Fig. 1) (25). This remarkable increase in PD is most prominent in the B -band, which shows the highest PD, between 2.5–5%, while the R -band polarization is in the range of 0.5–2%. The PA is most accurately determined and shows least variability in the B -band, with the average being $\text{PA} = -18.8 \pm 0.5$.

The detected quiescent-state polarization possesses three remarkable properties: its spectrum is blue with the frequency dependence $P_\nu \propto \nu^3$, the PD remains high and the PA is very stable. The PA shows some stochastic variations with an amplitude of $< 10^\circ$, but no apparent dependence on the orbital phase. These exceptional properties put tight constraints on the nature of the polarized emission. In order to understand the origin of polarization, we performed spectral modeling of the broadband photometric data obtained with the Liverpool Telescope (LT) and *Swift*/UVOT together with the polarized fluxes (table S3 and Fig. S2). We find that the total spectrum can be decomposed into three components: the companion star (contributing about 20% to the r -band flux), the multicolour accretion disk with the inner temperature $T_d \approx 6200$ K and the inner radius of $R_d \approx 6.5 \times 10^{10}$ cm, and an additional UV component, which can be described by a blackbody of temperature $T_{\text{bb}} \approx 15500$ K and radius $R_{\text{bb}} \approx 8 \times 10^9$ cm (25).

The jet cannot be the source of the polarized radiation because its energy distribution is expected to be red, contradicting the observed blue polarized spectrum, and also the PA is systematically offset by about 45° from the jet position angle. The absence of pronounced orbital variations of the PA also excludes hot spot origin. Finally, the standard optically thick accretion disk can also be excluded based on the high polarization degree and spectral dependence. A viable source of polarization is scattering of the accretion disk radiation, acting as a provider of the seed photons, in the hot advection-dominated flow (ADAF) close to the disk inner radius (25, 26). This model predicts polarization parallel to the meridional plane, the plane formed by the orbital axis and photon propagation direction. Another possibility is dust scattering, which is believed to be responsible for similarly blue polarized spectra observed from accretion disks around supermassive black holes in Seyfert galaxies and quasars (27–29). If the dust is located in a flattened envelope above the accretion disk, the polarization vector is also parallel to the meridional plane. However, if dust forms an extended structure at high elevation above the accretion disk, polarization is likely perpendicular to the meridional plane. In this model, however, the UV excess needs yet another explanation.

Independently of the spectral modeling and precise geometry, the stability of the PA over the orbital phase suggests the polarization is related to the orbital axis; either parallel or perpendicular to that. Hence, the observed PA gives information about the position angle of the orbital axis, the missing ingredient to measure the misalignment β between the black hole and orbital spin. It can be computed as

$$\cos \beta = \cos i_{\text{bh}} \cos i_{\text{orb}} + \sin i_{\text{bh}} \sin i_{\text{orb}} \cos \Delta, \quad (\text{S1})$$

where i_{bh} is the inclination of the black hole spin and $\Delta = \theta_{\text{bh}} - \theta_{\text{orb}}$ is the difference between the position angles of the black hole spin and the orbital angular momentum. If the black hole

spin is directed along the southern approaching jet, then its inclination $i_{\text{bh}} = i_{\text{jet}} = 63^\circ \pm 3^\circ$ and its position angle is $\theta_{\text{bh}} = 180^\circ + \theta_{\text{jet}} = 205.1 \pm 1.4$ (17–19). The smallest misalignment $\beta \approx 42^\circ$ is achieved when the orbital spin is also directed South at $\theta_{\text{orb}} = \text{PA} + 180^\circ = 161.2 \pm 0.5$ (because the PA is unique only modulo 180°), at the inclination $i_{\text{orb}} \approx 73^\circ$. The probability distribution for β in this case is shown in Fig. 2. The radial velocity measurements are not able to differentiate between orbital inclinations i_{orb} and $180^\circ - i_{\text{orb}}$, and the second option gives $\beta \approx 62^\circ$. If either the orbital angular momentum or the black hole spin is directed to the North instead, the black hole rotation is then retrograde, resulting in $\beta \approx 118^\circ$ or 138° for the two options of the orbital inclination.

If polarization is perpendicular to the meridional plane, the position angle of the orbital spin can take values $\theta_{\text{orb}} = \text{PA} + 90^\circ$ or $\text{PA} + 270^\circ$. This geometrical arrangement then results in $\beta \approx 44^\circ, 64^\circ, 116^\circ, 136^\circ$. All possible cases of the relative orientation of the black hole and orbital spins and the resulting values for β as well as the azimuthal angle of the black hole spin in the orbital plane are given in table S4 (25).

The observed difference of $\approx 44^\circ$ between the jet position angles and the PA gives the first direct observational evidence for a large, at least $\sim 40^\circ$, misalignment between the black hole spin and the orbital angular momentum. This result is highly robust and independent of the modeling details, as it relies only on one observed quantity: the polarization angle.

During the outbursts, such an extreme misalignment severely affects the accretion disk structure in the ultimate proximity of the black hole. For a non-zero spin, particles moving around the black hole in the orbits tilted, with respect to the black hole equatorial plane, undergo Lense-Thirring precession with the rate decreasing with radius. Hence, the tilted disk is subject to twist and warp. Evidence for a large misalignment challenges the models of quasi-periodic oscillations observed in black hole x-ray binaries, which rely on the solid-body Lense-Thirring precession of the inner parts of the accretion flow, as these imply the whole flow is misaligned by 2β from the orbital axis in some phases (3). For $\beta \sim 40^\circ$ this means that the inner parts of the accretion disk would need to become almost perpendicular to its outer parts.

So far, many models do not give full consideration to the case of a large misalignment, and much smaller angles have been assumed, typically, $\beta \sim 10^\circ - 20^\circ$ (3–5), although highly inclined possibilities with $\beta \sim 45^\circ - 65^\circ$ were also considered (30). Observational indications of the misalignment were put forward based on the gamma-ray light curves produced by the jet in Cyg X-3 (31), potentially high kick velocities of x-ray binaries acquired during formation (6), and the difference between orbital and jet inclination angles: about 15° in GRO J1655–40 (7) and even 50° in V4641 Sgr (32, 33). The precise value for misalignment in the latter case has a high spread and is, in general, strongly dependent on the underlying assumptions. We note that without information on the binary plane orientation, we could not have obtained the real, high misalignment angle in MAXI J1820+070, as the orbital inclination is only marginally different from the jet inclination. This highlights the important role of the polarimetric observations during quiescence.

Our finding proves observationally the need to treat the misalignment angle as a free parameter when measuring black hole masses and spins. This removes a systematic bias in-

roduced by assuming the black hole spin axis and the orbital angular momentum axes are aligned (13, 17, 34). The large degree of misalignment puts strong constraints on the supernova explosion and black hole formation mechanisms, as it can only decrease during the accretion stage (7). A large misalignment angle causes precession of the binary orbital plane and alters the waveforms of the gravitational wave signals (9). A fraction of detected gravitational wave signals from binary black holes indeed show signs of orbital precession (8). The conservation of a large misalignment angle up to the in-spiral phase can be the reason behind the systematically small effective spins and non-zero average effective precession spin parameter measured in merging black holes observed by LIGO/Virgo.

References

1. C. S. Reynolds, *Space Sci. Rev.* **183**, 277 (2014).
2. J. E. McClintock, R. Narayan, J. F. Steiner, *Space Sci. Rev.* **183**, 295 (2014).
3. P. C. Fragile, O. M. Blaes, P. Anninos, J. D. Salmonson, *Astrophys. J.* **668**, 417 (2007).
4. A. Ingram, C. Done, P. C. Fragile, *Mon. Not. R. Astron. Soc.* **397**, L101 (2009).
5. A. Veledina, J. Poutanen, A. Ingram, *Astrophys. J.* **778**, 165 (2013).
6. P. Atri, *et al.*, *Mon. Not. R. Astron. Soc.* **489**, 3116 (2019).
7. T. J. Maccarone, *Mon. Not. R. Astron. Soc.* **336**, 1371 (2002).
8. R. Abbott, *et al.*, *Astrophys. J. Lett.* **913**, L7 (2021).
9. T. A. Apostolatos, C. Cutler, G. J. Sussman, K. S. Thorne, *Phys. Rev. D* **49**, 6274 (1994).
10. R. D. Blandford, R. L. Znajek, *Mon. Not. R. Astron. Soc.* **179**, 433 (1977).
11. I. F. Mirabel, L. F. Rodríguez, *Ann. Rev. Astron. Astrophys.* **37**, 409 (1999).
12. J. Frank, A. King, D. J. Raine, *Accretion Power in Astrophysics: Third Edition* (Cambridge University Press, Cambridge, UK, 2002).
13. M. A. P. Torres, *et al.*, *Astrophys. J. Lett.* **893**, L37 (2020).
14. T. Kawamuro, *et al.*, *The Astronomer's Telegram* **11399**, 1 (2018).
15. D. Denisenko, *The Astronomer's Telegram* **11400** (2018).
16. M. A. Tucker, *et al.*, *Astrophys. J. Lett.* **867**, L9 (2018).
17. P. Atri, *et al.*, *Mon. Not. R. Astron. Soc.* **493**, L81 (2020).

18. J. S. Bright, *et al.*, *Nature Astronomy* **4**, 697 (2020).
19. M. Espinasse, *et al.*, *Astrophys. J. Lett.* **895**, L31 (2020).
20. V. Piirola, A. Berdyugin, S. Berdyugina, *Proc. SPIE, Vol. 9147, Ground-based and Airborne Instrumentation for Astronomy V* (2014), p. 91478I.
21. V. Piirola, I. A. Kosenkov, A. V. Berdyugin, S. V. Berdyugina, J. Poutanen, *Astron. J.* **161**, 20 (2021).
22. A. Veledina, *et al.*, *Astron. & Astrophys.* **623**, A75 (2019).
23. I. A. Kosenkov, *et al.*, *Mon. Not. R. Astron. Soc.* **496**, L96 (2020).
24. M. A. P. Torres, *et al.*, *Astrophys. J. Lett.* **882**, L21 (2019).
25. Materials and methods are available as supplementary materials.
26. R. Narayan, J. E. McClintock, I. Yi, *Astrophys. J.* **457**, 821 (1996).
27. G. Berriman, *Astrophys. J.* **345**, 713 (1989).
28. C. Brindle, *et al.*, *Mon. Not. R. Astron. Soc.* **244**, 604 (1990).
29. W. Webb, M. Malkan, G. Schmidt, C. Impey, *Astrophys. J.* **419**, 494 (1993).
30. M. Liska, *et al.*, *Mon. Not. R. Astron. Soc.* (2020).
31. A. A. Zdziarski, *et al.*, *Mon. Not. R. Astron. Soc.* **479**, 4399 (2018).
32. J. A. Orosz, *et al.*, *Astrophys. J.* **555**, 489 (2001).
33. G. Salvesen, S. Pokawanvit, *Mon. Not. R. Astron. Soc.* **495**, 2179 (2020).
34. X. Zhao, *et al.*, *arXiv e-prints* p. arXiv:2012.05544 (2020).
35. A. Berdyugin, V. Piirola, J. Poutanen, *Astronomical Polarisation from the Infrared to Gamma Rays*, R. Mignani, A. Shearer, A. Słowikowska, S. Zane, eds. (Springer Nature, Cambridge, 2019), vol. 460 of *ASSL*, pp. 33–65.
36. I. A. Kosenkov, *et al.*, *Mon. Not. R. Astron. Soc.* **468**, 4362 (2017).
37. Gaia Collaboration, *et al.*, *Astron. & Astrophys.* **616**, A1 (2018).
38. K. Serkowski, *Advances in Astronomy and Astrophysics* **1**, 289 (1962).
39. I. A. Steele, *et al.*, *Proc. SPIE, Vol. 5489, Ground-based Telescopes*, J. Oschmann, Jacobus M., ed. (2004), pp. 679–692.

40. J. L. Tonry, *et al.*, *Astrophys. J.* **750**, 99 (2012).
41. N. Gehrels, *et al.*, *Astrophys. J.* **611**, 1005 (2004).
42. P. A. Evans, *et al.*, *Mon. Not. R. Astron. Soc.* **397**, 1177 (2009).
43. K. A. Arnaud, *Astronomical Data Analysis Software and Systems V*, G. H. Jacoby, J. Barnes, eds. (ASP, San Francisco, 1996), vol. 101 of *ASP Conf. Ser.*, pp. 17–20.
44. P. Bharali, J. Chauhan, K. Boruah, *Mon. Not. R. Astron. Soc.* **487**, 5946 (2019).
45. P. J. Brown, A. Breeveld, P. W. A. Roming, M. Siegel, *Astron. J.* **152**, 102 (2016).
46. J. A. Cardelli, G. C. Clayton, J. S. Mathis, *Astrophys. J.* **345**, 245 (1989).
47. P. Predehl, J. H. M. M. Schmitt, *Astron. & Astrophys.* **293**, 889 (1995).
48. C. S. Froning, *et al.*, *Astrophys. J.* **743**, 26 (2011).
49. A. J. Pickles, *Pub. Astron. Soc. Pacific* **110**, 863 (1998).
50. S. Chandrasekhar, *Radiative Transfer* (Dover, New York, 1960).
51. V. V. Sobolev, *A Treatise on Radiative Transfer* (Van Nostrand, Princeton, 1963).
52. G. B. Rybicki, A. P. Lightman, *Radiative Processes in Astrophysics* (Wiley, New York, 1979).
53. G. Wardziński, A. A. Zdziarski, *Mon. Not. R. Astron. Soc.* **325**, 963 (2001).
54. A. Veledina, J. Poutanen, I. Vurm, *Mon. Not. R. Astron. Soc.* **430**, 3196 (2013).
55. V. L. Ginzburg, S. I. Syrovatskii, *Ann. Rev. Astron. Astrophys.* **7**, 375 (1969).
56. R. A. Sunyaev, L. G. Titarchuk, *Astron. & Astrophys.* **143**, 374 (1985).
57. F. Yuan, R. Narayan, *Ann. Rev. Astron. Astrophys.* **52**, 529 (2014).
58. J. Poutanen, R. Svensson, *Astrophys. J.* **470**, 249 (1996).
59. J. Poutanen, *Astrophys. J. Suppl. Ser.* **92**, 607 (1994).
60. J. S. Miller, R. W. Goodrich, W. G. Mathews, *Astrophys. J.* **378**, 47 (1991).
61. R. W. Goodrich, J. S. Miller, *Astrophys. J.* **434**, 82 (1994).
62. M. Kishimoto, *et al.*, *Nature* **454**, 492 (2008).
63. R. I. Hynes, *The Physics of Cataclysmic Variables and Related Objects*, B. T. Gänsicke, K. Beuermann, K. Reinsch, eds. (ASP, San Francisco, 2002), vol. 261 of *ASP Conf. Ser.*, pp. 676–677.

Acknowledgements

Acknowledgments: This paper is based on observations made with the Nordic Optical Telescope, owned in collaboration by the University of Turku and Aarhus University, and operated jointly by Aarhus University, the University of Turku, and the University of Oslo, representing Denmark, Finland, and Norway, the University of Iceland and Stockholm University at the Observatorio del Roque de los Muchachos, La Palma, Spain, of the Instituto de Astrofísica de Canarias. We thank the NOT staff for the excellent support. DIPol-UF is a joint effort between University of Turku (Finland) and Leibniz Institute for Solar Physics (Germany). We are grateful to the Institute for Astronomy, University of Hawaii for the observing time allocated for us at the Tohoku 60-cm telescope (T60) at Haleakala observatory. The Liverpool Telescope is operated on the island of La Palma by Liverpool John Moores University in the Spanish Observatorio del Roque de los Muchachos of the Instituto de Astrofísica de Canarias with financial support from the UK Science and Technology Facilities Council. **Funding:** The research leading to these results received funding from Magnus Ehrnrooth foundation and ERC Advanced Grant HotMol ERC-2011- AdG-291659. A.V. acknowledges support from the Academy of Finland grant 309308. J.P., A.V., V.K., and S.S.T. received funding from the Russian Science Foundation grant 20-12-00364. M.A.P.T. acknowledges support from the State Research Agency (AEI) of the Spanish Ministry of Science, Innovation and Universities (MCIU) and the European Regional Development Fund (FEDER) under grant AYA2017-83216-P and via a Ramón y Cajal Fellowship (RYC-2015-17854). **Author contributions:** J.P. and A.V. suggested the idea for the project, performed modeling and wrote most of the text. A.V.B., V.P., and I.K. have developed DIPol-UF and the data analysis software, planned and performed polarimetric observations. H.J., M.S. and M.A.P.T. planned and executed observations at the Liverpool Telescope and VK reduced the photometric data. J.J.E.K. proposed the Swift observations and analysed the data together with S.S.T. P.G.J. and S.V.B. contributed to interpretation of results. All authors provided input and comments on the manuscript. **Competing interests:** The authors declare no conflicts of interest. **Data and materials availability:** The Liverpool Telescope data are available from its data archive at <https://telescope.livjm.ac.uk/DataProd/>. The Swift observatory data are available through the NASA data archive at <https://heasarc.gsfc.nasa.gov>. The DIPol-UF data are available in table S1.

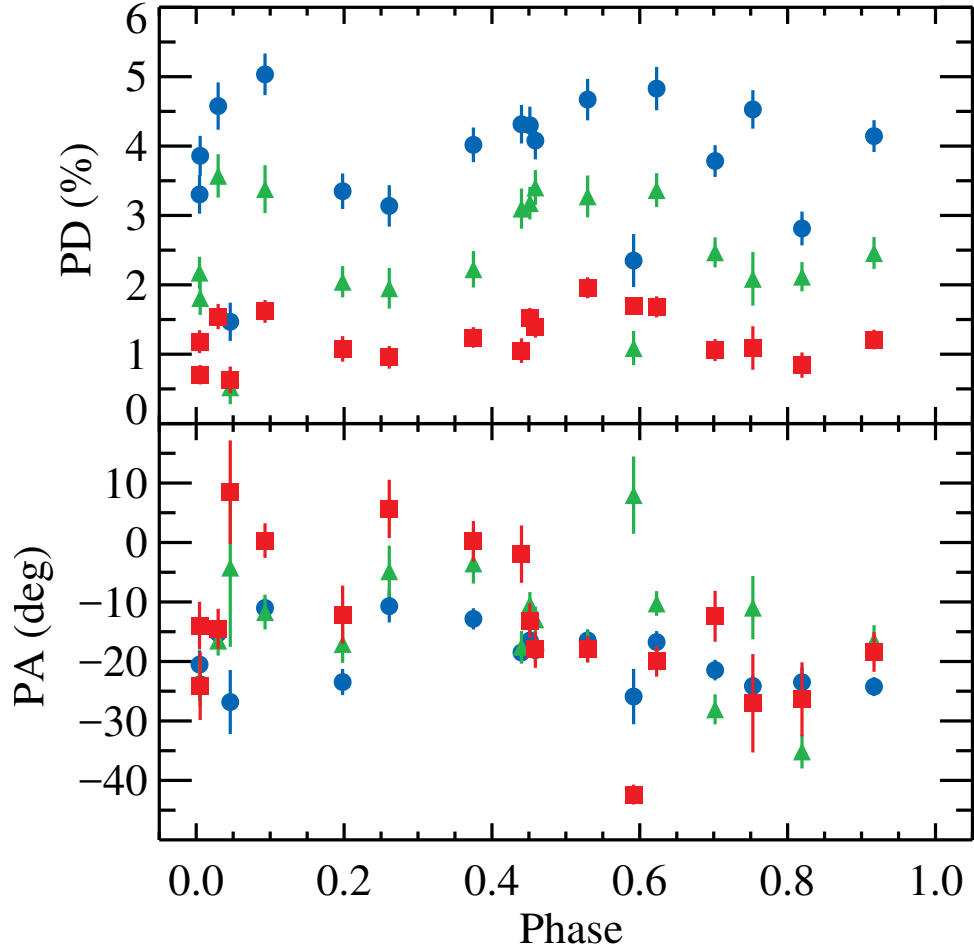


Figure 1: Polarization properties of MAXI J1820+070. Intrinsic polarization degree (PD) and polarization angle (PA) of MAXI J1820+070 in quiescence are shown as a function of orbital phase using ephemeris from ref. (24). Blue circles, green triangle and red squares correspond to three bands: *B*, *V*, and *R*, respectively.

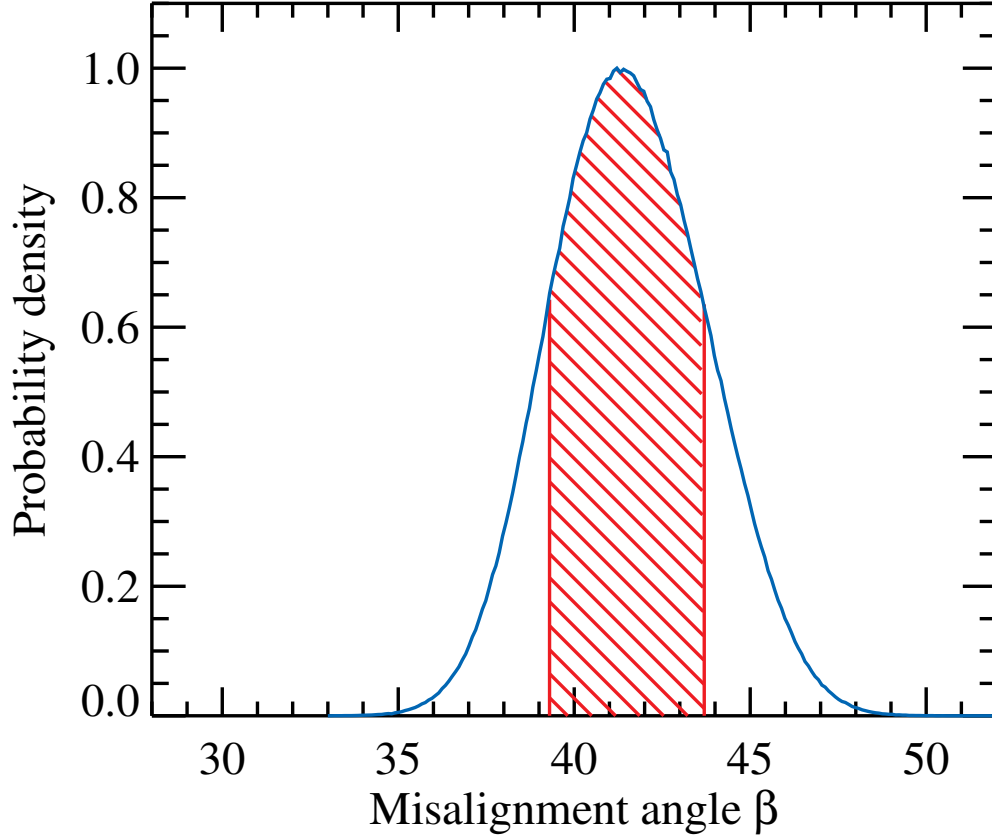


Figure 2: Probability distribution function for the misalignment angle. Probability distribution function for the smallest misalignment angle between the black hole and orbital spins is shown. This case corresponds to the black hole spin directed along the southern approaching jet and the orbital spin being directed also to the South at a position angle $\theta_{\text{orb}} = \text{PA} + 180^\circ$ and inclination $\approx 73^\circ$. The red hatched region corresponds to the 68% confidence interval (i.e. between 16th and 84th percentiles of the posterior distribution).

Supplementary Materials

This PDF file includes

Materials and Methods

Figures S1 to S6

Tables S1 to S4

References (36-64)

Materials and Methods

DIPol-UF/NOT observations

We have performed polarimetric observations of the black hole x-ray binary MAXI J1820+070 both during the bright stages of the outburst as well as in the quiescence. The data during the outburst (22, 23) were obtained with the DIPol-2 polarimeter (20) mounted on the Tohoku 60-cm telescope (T60) at Haleakala observatory, Hawaii. During the quiescence MAXI J1820+070 was observed with the new Double Image Polarimeter Ultra Fast (DIPol-UF) (21) at the 2.5 m Nordic Optical Telescope (NOT) in July 2019 (commissioning run), April and July 2020 (see Fig. 1 and Table S1). Both polarimeters have similar design: incoming light passes through a modulator (superachromatic half-wavelength plate, HWP), it is then split by the plane-parallel calcite plate into two orthogonally polarized rays (ordinary and extraordinary) and further is reflected by two dichroic beam splitters to produce o- and e-images on three CCDs simultaneously in the B , V , R bands. This design allows to optically eliminate the sky polarization at the registration stage (even if it is variable), and to achieve unprecedentedly high, up to 10^{-5} , accuracy of target polarimetric measurements. The instrumental polarization below 10^{-4} level is accounted for by using zero-polarization standards and is completely negligible for the purpose of the present paper. The zero point of PA was determined by observing high polarization standards.

For one independent measurement of linear polarization four sequential images with HWP rotated by 22.5° in each step are obtained. One measurement cycle consists of 16 images recorded simultaneously by three CCDs for one full rotation of the HWP modulator (0° – 360°) giving four independent measurements of the normalized Stokes parameters (q, u) in the B , V , and R bands. This algorithm provides the best accuracy and helps eliminate effects arising from dust particles on the retarder, nonparallelism of rotating components, etc. The images produced by DIPol-UF require standard CCD calibrations (35).

The average normalized Stokes parameters (q, u) are then obtained from 16 to 40 individual measurements using so-called 2σ weighting algorithm (21, 36). The typical duration of an observational window where the data were averaged was one hour. The polarization produced by the interstellar medium (ISM) has been estimated from numerous (more than 400) observations of sample of the field stars (stars #2, 3, 6, 7, 9 from fig. 9 of ref. (22)), which are close in distance to the target as probed by *Gaia* parallaxes (37). These normalized Stokes parameters

$(q_{\text{ISM}}, u_{\text{ISM}})$ were subtracted from the measured values of the normalized Stokes parameters to obtain the intrinsic polarization information of the source $(q_{\text{intr}}, u_{\text{intr}})$. We then define the complex linear polarization quantity as $\mathcal{P} = q_{\text{intr}} + iu_{\text{intr}}$. Intrinsic polarization degree (PD) P and polarization angle (PA) θ are then obtained by standard formulae

$$P = |\mathcal{P}| = \sqrt{q_{\text{intr}}^2 + u_{\text{intr}}^2}, \quad \theta = \frac{1}{2} \arg(\mathcal{P}). \quad (\text{S2})$$

Because our measurements typically have significance 5–10 σ , the bias in the measured PD is negligible and the error in PD ΔP is the same as the error on individual Stokes parameters. The error of the PA is estimated as $\Delta\theta = \Delta P/(2P)$ (38). The intrinsic PD and PA computed following this procedure are reported in Table S1.

No clear dependence on the orbital phase was found (see Fig. 1). The PD has a very blue spectrum $P_\nu \propto \nu^3$, inconsistent with the red spectra expected from the jet or accretion disk. The PA is very stable in the B -band where the PA is the highest and the relative error is smallest. The average PA in that band obtained by averaging individual PA was -18.8 ± 0.5 . The PA computed from the averaged Stokes parameters was very similar: -19.1 ± 0.5 .

Using images from DIPol-UF we have also obtained photometry of MAXI J1820+070 relative to two nearby stars (#1 and 2 from table 2 in ref. (22)). Absolute photometry was obtained using simultaneous observations by the LT. The flux of MAXI J1820+070 in all bands is anti-correlated with the PD (see Fig. S1). This anti-correlation together with the spectral dependence of the PD can be interpreted as an interplay between two components: one, non-polarized, variable component dominating the flux in the red, and another, polarized, with contribution growing towards blue.

Liverpool Telescope observations

Photometric observations in the optical band were performed using the IO:O instrument with the SDSS-*irz*, Bessel V and B filters on the LT (39) on La Palma, Spain. The object was observed during four nights from 2020 July 20 to 24 (MJD 59050–59054). LT image reduction was provided by the basic IO:O pipeline. As the photometric standards, we used four stars with known Pan-STARRS1 (PS1) PSF magnitudes. To convert PS1 magnitudes to SDSS and Johnson-Cousins magnitudes we used equation (6) and Table 6 from ref. (40). To obtain fluxes of the object from its magnitudes we used standard zero-points for SDSS and Johnson-Cousins systems. The fluxes and their errors are presented in Table S2.

Swift/UVOT observations

The *Neil Gehrels Swift Observatory* (*Swift*) (41) observed MAXI J1820+070 in the low state with the XRT and UVOT instruments (partly quasi-simultaneously with DIPol-UF/NOT) between 2020 July 20 – September 6. All the XRT data were taken in the photon counting

mode with about 9 ks of total exposure. An averaged spectrum was extracted using the on-line tools (42) provided by the UK Swift Science Data Centre. The spectrum was rebinned to have at least 1 count per energy channel. The data were fitted in the 0.5–10 keV band using the XSPEC package (43) with an absorbed power-law model TBABS*POWERLAW. Fixing the hydrogen column to $N_{\text{H}} = 1.6 \times 10^{21} \text{ cm}^{-2}$ (44) we obtained the power-law photon index $\Gamma = 1.62 \pm 0.24$ with C-Stat = 42.7 for 46 degrees of freedom. We find flux corrected for absorption of $(3.3 \pm 0.7) \times 10^{-13} \text{ erg cm}^{-2} \text{ s}^{-1}$ in the 0.5–10 keV energy range.

The UVOT data were processed with the UVOTPRODUCT tool. We used a 5'' source aperture around the known Gaia position of MAXI J1820+070, and a circular source-free 10'' background aperture about 40'' east of it. After comparing the magnitudes obtained between July 20 – September 6 to other quiescence data taken when the x-ray counting rate was low, we noted that during this period MAXI J1820+070 was roughly 0.5–1 magnitude fainter in all the UV filters than in the data taken in 2019 or earlier in 2020, the same trend was observed in the V-band and, to a lesser extent, in the R-band. Therefore, we decided to stack all the 2020 July 20–September 6 UVOT data together to obtain time averaged fluxes in the u, uvw1, uvm2 and uvw2 filters for the spectral energy distribution (SED). Conversion of the background corrected count rates obtained from the UVOTPRODUCT to the fluxes is non-trivial, as it depends on the assumed spectral shape (45). Therefore, for reliable estimate of the fluxes we performed direct spectral fitting with a broad-band SED model using the XSPEC package.

Decomposition of the broadband spectrum

The broad-band average spectrum obtained with the LT and *Swift*/UVOT is presented in Fig. S2. The spectrum is corrected for reddening using model of ref. (46) with $A_V = 0.89$ (corresponding to $E(B - V) = 0.29$) obtained from the measured hydrogen column density $N_{\text{H}} = (0.16 \pm 0.02) \times 10^{22} \text{ cm}^{-2}$ (44) using transformation $A_V = 5.59 N_{\text{H}}/10^{22} \text{ cm}^{-2}$ (47). The optical/infrared spectrum obtained with the LT is very red and can approximately be described by a model of multicolour disk (dotted line), but the UVOT data show a clear UV excess. The excess is also seen in the non-dereddened data and is not an artefact of dereddening procedure. Similar excess has been detected previously in the quiescent-state *HST* data of the black hole x-ray binary A 0620–00 (48), but its nature remained a mystery. In order to describe the excess, we added a phenomenological blackbody model (dashed line). In addition, the spectroscopic data obtained during quiescence demonstrate the presence of a K4-K5 V companion star (13, 24) which contributed about 20% to the flux in the R-band.

The detected blue PD spectrum, roughly $P_{\nu} \propto \nu^3$, is drastically different from the red (even after correcting for the reddening) spectrum of the infrared to UV continuum. This argues against accretion disk as the source of polarized light. Instead, it is likely that the component producing the UV excess is responsible for polarization. To extract the average shape of the polarized component, we calculated the polarized fluxes (PF) as

$$PF_k = P_k F_k, \quad (\text{S3})$$

where k is the index corresponding to one of the BVR -bands, P_k is the average PD and F_k is the average flux in this band. If PD of the polarized component is wavelength-independent, then the computed PF directly replicates its total spectral shape, while fluxes being smaller by the polarization fraction. The average PD was computed from the averaged Stokes parameters obtained in 18 individual measurements during quiescence with DIPol-UF (see Table **S1**). Because absolute photometry with DIPol-UF is not very reliable, the average flux was obtained from the LT observations. Averaging PF of individual observations produces nearly identical results.

Using XSPEC v.12.11, we perform spectral fitting of the total spectrum from LT and *Swift*/UVOT and, jointly, the three points of the PF. The total spectrum is described by the model REDDEN (BBODYRAD+DISKBB+BBODYRAD). The REDDEN model describes interstellar extinction (46). The first BBODYRAD corresponds to the spectrum of the K4 V stellar companion, modeled by a blackbody of fixed temperature $T_* = 4500$ K and radius $R_* = 5 \times 10^{10}$ cm, which is a good approximation to the actual spectrum of such a star from the atlas of ref. (49) (compare pink dot-dashed and green solid curves in Fig. **S2**). The DISKBB corresponds to the multicolour accretion disk. It has two free parameters: normalization, which is related to the inner radius R_{in} , and temperature at that radius T_{in} . Normalizations were converted to radii assuming the distance to the source of 2.96 kpc as determined by the radio parallax (17) and disk inclination $i_{\text{orb}} = 70^\circ$ (13). The second BBODYRAD corresponds to the UV excess that is modeled by a blackbody with two free parameters: temperature T_{bb} and radius R_{bb} . The PF is modeled by the reddened second blackbody only with an additional factor P_{UV} . The best-fitting parameters are listed in Table **S3**.

We find the accretion disk temperature of about 6200 K, which is very close to that expected for the disk in quiescence (12). The inner radius of the disk is $\approx 6.3 \times 10^{10}$ cm, which is just 20% smaller than the circularization radius for a companion-to-black hole mass ratio of $q = 0.072$ and 16.87 h orbital period (13). The outer radius has to be at least 2–3 times larger not to underpredict the red part of the spectrum. This is consistent with the expectation that the accretion disk size does not exceed the tidal radius of about 2.4×10^{11} cm.

The temperature of the additional blackbody is $T_{\text{bb}} \sim 15500$ K and the characteristic size 8×10^9 cm. It reproduces the shape of the polarized flux spectrum and matches well the UV excess. The PD of this component is $P_{\text{UV}} = 0.062^{+0.026}_{-0.014}$, corresponding to 5–9% intrinsic PD (on average) of the polarized component. The broad-band spectrum and the best-fitting spectral components are shown in Fig. **S2**. The computed values of PF were divided by the constant P_{UV} to demonstrate the fit with the UV excess component.

For lower and higher value of the colour excess of 0.25 and 0.325, corresponding to the 1σ uncertainties in N_{H} , the best-fitting spectral parameters change somewhat. A lower $E(B - V)$ leads to the 7% smaller disk temperature T_{in} and 10% larger inner radius R_{in} , 7% smaller blackbody temperature T_{bb} and 2% larger radius R_{bb} . For a higher $E(B - V)$, the effect is opposite: T_{in} is 5% larger, R_{in} is 7% smaller, T_{bb} is 7% larger and R_{bb} is smaller by 2%. This uncertainty does not affect any of our conclusions.

The source of polarized light and the nature of the spectral components

Our data pose two questions: what is the nature of the UV excess and what is the source of polarized radiation. The accretion disk itself is not the source of the UV emission, because in quiescence its temperature is lower as we see from the red optical spectrum. Another possibility is a hotspot (or hot line), the place where the accretion stream hits the disk. This component can be responsible for the UV excess. However, whether it can also be the source of polarization is questionable. The high temperature of this component implies that the matter is ionized. The PD from the optically thick electron-scattering dominated atmosphere (50, 51) depends on the cosine of the viewing angle $\mu = \cos i_{\text{orb}}$ approximately as $11.7\% \times (1 - \mu)/(1 + 3.582\mu)$. For inclination angles permitted by the absence of eclipses (13), $i_{\text{orb}} < 81^\circ$, the expected PD is $\lesssim 6\%$. A high implied PD, $P_{\text{UV}} \approx 5\text{--}9\%$, is barely consistent with that.

On the other hand, high PD can be produced by the synchrotron radiation in the ordered magnetic field. Blue spectrum indicates that we might see the optically thick part of this radiation, with the possible transition to optically thin part at $\nu \gtrsim 10^{15}$ Hz. Self-absorption becomes important at the turn-over frequency (52–54), $\nu_t \approx 3 \times 10^{15} B_6^{\frac{p+2}{p+4}} (\tau_t \gamma_t^p)^{\frac{2}{p+4}}$, where B_6 is the magnetic field in units of 10^6 G, τ_t is the Thomson optical depth of electrons emitting at the turn-over frequency, γ_t is their Lorentz factor and p is the power-law index of electron distribution, $dn_e/d\gamma \propto \gamma^{-p}$. For the observed $\nu_t \approx 10^{15}$ Hz, this requires highly opaque source and/or high magnetic field, which can be expected in the bright hard state, but inconsistent with the relevant values for the source in (near-)quiescence. The highest theoretically possible PD below the self-absorption frequency (55) of $P_{\text{max}} = 3/(6p + 13) \sim 0.1$ requires highly ordered – and constant – magnetic field during the whole year July 2019– July 2020. Hence, we find the synchrotron radiation to be an implausible source of the observed polarized flux.

Further, a substantial polarization may be produced by electron scattering of radiation in an optically thin slab if the seed photons are injected along the slab plane (56). The PD = $(1 - \mu^2)/(3 - \mu^2)$ reaches 33% edge-on and is a weak function of orbital inclination (for $i_{\text{orb}} \gtrsim 66^\circ$, i.e. $\cos i_{\text{orb}} \lesssim 0.41$, the PD is larger than $\sim 30\%$). Scattering in the Thomson regime means that the scattered radiation does not gain a systematic shift in energy with respect to the incident continuum, and hence the peak of the spectrum of the polarized component directly probes the characteristic energy and spectral shape of the incident radiation. Hence, the source of the incident light should have narrow, blackbody-like shape, with characteristic temperature $T \sim 16000$ K. Because this temperature is much higher than the disk inner temperature, and the polarization angle is independent of orbital phase, the location and physical properties of such a component are unclear.

The additional polarized component may instead be coming from Compton up-scattering of soft photons by hot electrons, which is related to a systematic shift in energy. Hot, optically thin ADAF may exist in low-luminosity black hole binaries and active galactic nuclei (26, 57). Alternatively, a hot layer (corona) atop of the cold disk, heated by the unwinding stream of matter, may exist. In both cases, the hot medium is expected to be optically thin, and may Compton up-scatter the photons coming from the cold accretion disk. We calculate the spectra and po-

larization properties of Compton scattering following the formalism presented in ref. (58). We assume the spectrum of incident, non-polarized photons is a blackbody with temperature equal to the disk inner temperature $T_{\text{bb}} = 6200$ K. For these seed photons, to get the peak of the first scattering order at $\sim 10^{15}$ Hz (as demanded by the spectral decomposition), we need to have electrons with temperature of about 200 keV. For such a high temperature, the PD is expected to drop with respect to the maximal, Thomson-regime PD by a factor of 3 (59). In the case of inner hot flow, only the photons travelling at large enough inclinations $\alpha > \alpha_{\text{crit}}$ to the disk normal can interact with the hot matter. This limiting angle is related to the scale-height of the hot medium $\cot \alpha_{\text{crit}} \sim (H/R)$. Increasing the flow scale-height leads to a drop of PD. In Fig. S5 we show the resulting flux, polarized flux and PD spectra at different viewing angles $i_{\text{orb}} = 66^\circ$, 73° and 81° . Note that in this case the polarization is parallel to the disk normal. We see that the PD of scattered radiation is nearly independent of the photon frequency up to its peak at $\nu \sim 10^{15}$ Hz and therefore the spectral shape of the flux and PF of the scattered component are nearly identical in the optical band.

For the slab-corona geometry, an appropriate parameter determining PD is the Thomson optical depth of the hot slab τ_{T} . Only for $\tau_{\text{T}} \gtrsim 0.5$ a significant polarization exceeding 5% can be produced and the dominant electric-field oscillations are perpendicular to the projection of the disk normal. However, Comptonization in a slab of $\tau_{\text{T}} = 0.1$ and $kT_e = 200$ keV already overproduces the observed x-ray flux. This would imply that a more probable model that is better consistent with the observed spectral energy distribution and polarization properties is scattering of the disk radiation in the inner hot flow. Such a geometry favors an option that the measured PA is parallel to the orbital axis.

Finally, the blue PD spectrum can be produced by dust scattering of the accretion disk radiation. This process is believed to be responsible for similarly blue polarization spectra observed from supermassive black holes in Seyfert galaxies and quasars (27–29, 60–62). The dust can be located in a flattened envelope (equatorial wedge) around the accretion disk (61), or in an extended structure above the disk. These two cases predict different direction of polarization vector: parallel to the meridional plane in the first case, and perpendicular in the second. The dust scattering model, however, does not explain the UV excess. In order to make a more definite conclusion about the nature of polarized component, high signal-to-noise spectropolarimetric observations are needed to measure polarization in spectral lines.

Geometry

Here we define the coordinate systems and derive the necessary formulae to compute misalignment angle between the black hole spin and the orbital angular momentum as well as the azimuthal angle of the black hole spin projection in the orbital plane. Let us consider a Cartesian system with the $x - y$ plane coinciding with the orbital plane. Thus the unit vector of the orbital momentum is $\hat{\Omega} = (0, 0, 1)$. We choose the direction to an observer to lie in the $x - z$ plane at inclination angle i_{orb} as measured from the orbital axis (see Fig. S4 for geometry), so

that the observer unit vector is

$$\hat{\boldsymbol{o}} = (\sin i_{\text{orb}}, 0, \cos i_{\text{orb}}). \quad (\text{S4})$$

We assume that the black hole spin is directed at an angle β from the z -axis at azimuthal angle Φ_{bh} , which is measured from the x -axis in the counter-clockwise direction in the $x - y$ plane as viewed from the top. The unit vector of the black hole spin is

$$\hat{\boldsymbol{s}} = (\sin \beta \cos \Phi_{\text{bh}}, \sin \beta \sin \Phi_{\text{bh}}, \cos \beta). \quad (\text{S5})$$

Let us define the polarization basis with the unit vector $\hat{\boldsymbol{e}}_1$ directed on the sky in the direction of the projection of the orbital spin, vector $\hat{\boldsymbol{e}}_2$ being directed to the left on the sky, and the third vector coincides with the observer direction:

$$\begin{aligned} \hat{\boldsymbol{e}}_1 &= \frac{\hat{\boldsymbol{\Omega}} - \cos i_{\text{orb}} \hat{\boldsymbol{o}}}{\sin i_{\text{orb}}} = (-\cos i_{\text{orb}}, 0, \sin i_{\text{orb}}), \\ \hat{\boldsymbol{e}}_2 &= (0, -1, 0), \\ \hat{\boldsymbol{e}}_3 &= \hat{\boldsymbol{o}}. \end{aligned} \quad (\text{S6})$$

In this vector basis, the black hole and the orbital spin vectors can be represented as

$$\hat{\boldsymbol{s}} = (\sin i_{\text{bh}} \cos \Delta, \sin i_{\text{bh}} \sin \Delta, \cos i_{\text{bh}}), \quad (\text{S7})$$

$$\hat{\boldsymbol{\Omega}} = (\sin i_{\text{orb}}, 0, \cos i_{\text{orb}}) \quad (\text{S8})$$

where $\Delta = \theta_{\text{bh}} - \theta_{\text{orb}}$ is the difference in position angles of the black hole and the orbital spins. The misalignment angle β between the black hole and the orbital axis is then given by the scalar product:

$$\cos \beta = \hat{\boldsymbol{\Omega}} \cdot \hat{\boldsymbol{s}} = \cos i_{\text{bh}} \cos i_{\text{orb}} + \sin i_{\text{bh}} \sin i_{\text{orb}} \cos \Delta. \quad (\text{S9})$$

The direction cosines of the black hole spin vector $\hat{\boldsymbol{s}}$ in polarization basis are

$$\begin{aligned} \hat{\boldsymbol{s}} \cdot \hat{\boldsymbol{e}}_1 &= \sin i_{\text{bh}} \cos \Delta = \cos \beta \sin i_{\text{orb}} - \sin \beta \cos i_{\text{orb}} \cos \Phi_{\text{bh}}, \\ \hat{\boldsymbol{s}} \cdot \hat{\boldsymbol{e}}_2 &= \sin i_{\text{bh}} \sin \Delta = -\sin \beta \sin \Phi_{\text{bh}}, \\ \hat{\boldsymbol{s}} \cdot \hat{\boldsymbol{e}}_3 &= \cos i_{\text{bh}} = \cos \beta \cos i_{\text{orb}} + \sin \beta \sin i_{\text{orb}} \cos \Phi_{\text{bh}}, \end{aligned} \quad (\text{S10})$$

allowing us to obtain the azimuthal angle of the black hole spin:

$$\begin{aligned} \cos \Phi_{\text{bh}} &= \frac{\sin i_{\text{orb}} \cos i_{\text{bh}} - \cos i_{\text{orb}} \sin i_{\text{bh}} \cos \Delta}{\sin \beta}, \\ \sin \Phi_{\text{bh}} &= -\frac{\sin i_{\text{bh}} \sin \Delta}{\sin \beta}. \end{aligned} \quad (\text{S11})$$

We assume that the black hole spin is aligned with the jet. If the spin is directed along the southern approaching jet, then its inclination $i_{\text{bh}} = i_{\text{jet}} = 63^\circ \pm 3^\circ$ and its position angle is

$\theta_{\text{bh}} = 180^\circ + \theta_{\text{jet}} = 205.1 \pm 1.4$ (17–19). If, on the other hand, the black hole spin points along the northern receding jet, then $i_{\text{bh}} = 180^\circ - i_{\text{jet}} = 117^\circ \pm 3^\circ$ and its position angle is $\theta_{\text{bh}} = \theta_{\text{jet}} = 25.1 \pm 1.4$.

The polarimetric data provide us with the polarization angle $\text{PA} = -18.8 \pm 0.5$, which carries information about orientation of the orbital axis on the sky. If dominant oscillations of the electric field lie in the meridional plane formed by the orbital spin and photon propagation direction, the position angle of the orbital spin can be either $\theta_{\text{orb}} = \text{PA}$ or $\text{PA} + 180^\circ$. The electric field oscillations can also be perpendicular to the meridional plane, then the orbital spin position angle is $\text{PA} + 90^\circ$ or $\text{PA} + 270^\circ$. Furthermore, the radial velocity measurements are not able to differentiate between inclinations i_{orb} and $180^\circ - i_{\text{orb}}$. All possibilities result in 16 different geometrical arrangements of the black hole and orbital spins that satisfy observational constraints. These 16 cases are in reality reduced to eight different values for the misalignment angle β : four for misalignment less than 90° and four for misalignment between 90° and 180° for the retrograde rotation of the black hole (see Table S4).

The probability distribution for the orbital inclination i_{orb} was assumed to be a Gaussian with the peak at 73° with 1σ error of 6° and a cutoff at 81° (13, 24). For an alternative case of inclination exceeding 90° , the distribution symmetric relative to 90° is considered. Other parameters are assumed to follow a Gaussian distribution with corresponding 1σ errors. Using Monte-Carlo simulations, we obtain the probability distributions for β and Φ_{bh} using Equations (S9) and (S11), respectively. Their mean and standard deviation are given in Table S4.

As an illustration, in Fig. 2 we show the posterior probability distribution for β for the case of the smallest misalignment between the black hole and orbital spins. This particular case corresponds to the black hole spin directed along the southern approaching jet and the orbital spin being directed to the South at $\theta_{\text{orb}} = \text{PA} + 180^\circ$ and inclination $i_{\text{orb}} \sim 73^\circ$. The corresponding probability distribution for Φ_{bh} is shown in Fig. S3 and the illustration of the geometry in Fig. S6.

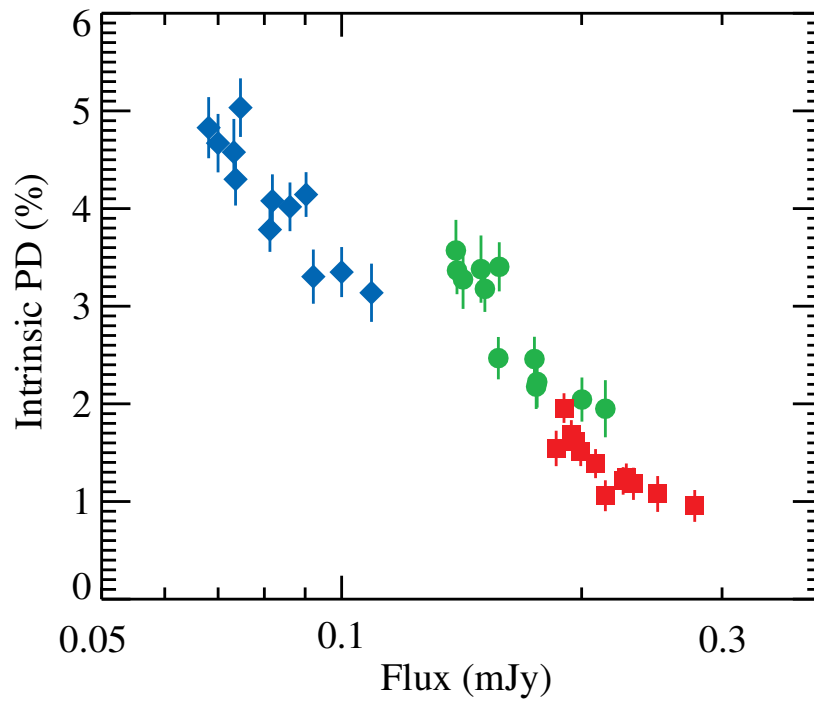


Figure S1: Dependence of the polarization on flux. An anti-correlation is shown between the observed flux (not corrected for reddening) and intrinsic source PD in three bands (B – blue diamonds, V – green circles, R – red squares) for the July 2020 observations of MAXI J1820+070.

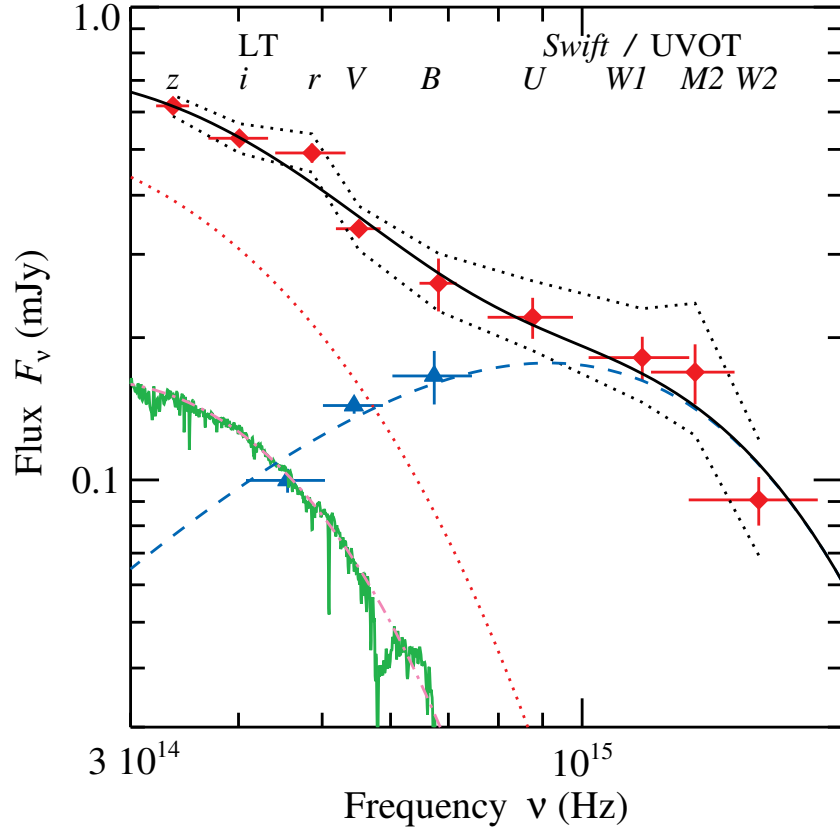


Figure S2: Spectral energy distribution (SED). Shown is the average SED of MAXI J1820+070 (red diamonds) as observed by the LT and *Swift*/UVOT telescope and corrected for reddening with colour excess $E(B - V) = 0.29$. The black dotted lines give the upper/lower limits on the flux for lower/higher extinction with $E(B - V) = 0.25$ and 0.325 , respectively. The polarized flux divided by the best-fitting polarization degree $P_{UV} = 0.062$ (i.e. multiplied by a factor of ~ 16) is shown with blue triangles. The black line gives the total model consisting of the companion star (pink dot-dashed line), accretion disk (red dotted) and a hot blackbody (blue dashed). The observed spectrum of a K4 V star from the atlas of ref. (49) is shown in green for comparison.

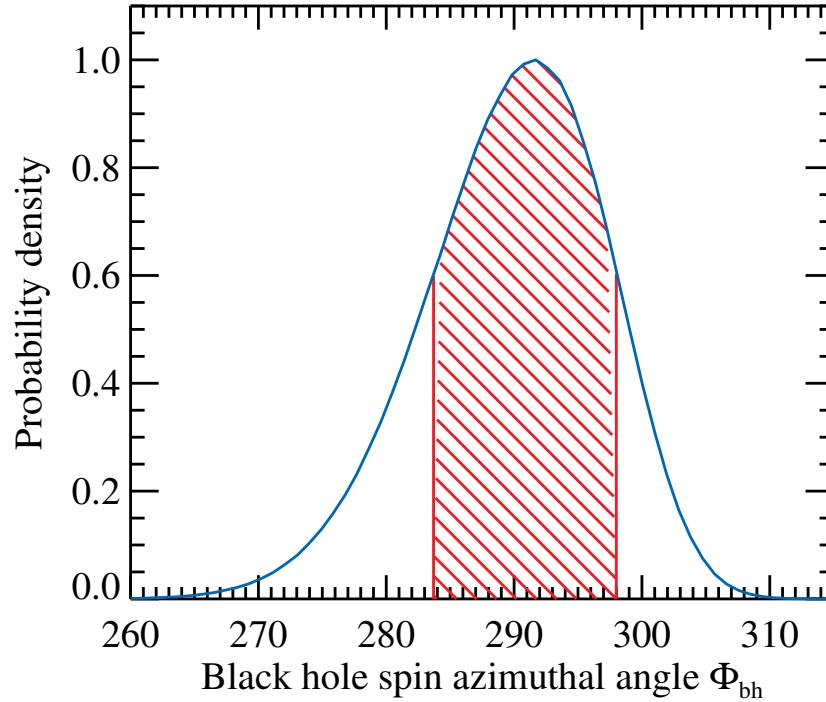


Figure S3: Probability distribution function for the black hole spin azimuthal angle. Shown is the probability distribution function for the black hole spin azimuthal angle Φ_{bh} in the case of the smallest misalignment between the black hole and orbital spins from Fig. 2. This geometry corresponds to the black hole spin directed along the southern approaching jet and the orbital spin being directed also to the South at position angle $\theta_{\text{orb}} = \text{PA} + 180^\circ$ and inclination $\approx 73^\circ$. The red hatched region corresponds to the 68% confidence interval (i.e. between 16th and 84th percentiles of the posterior distribution).

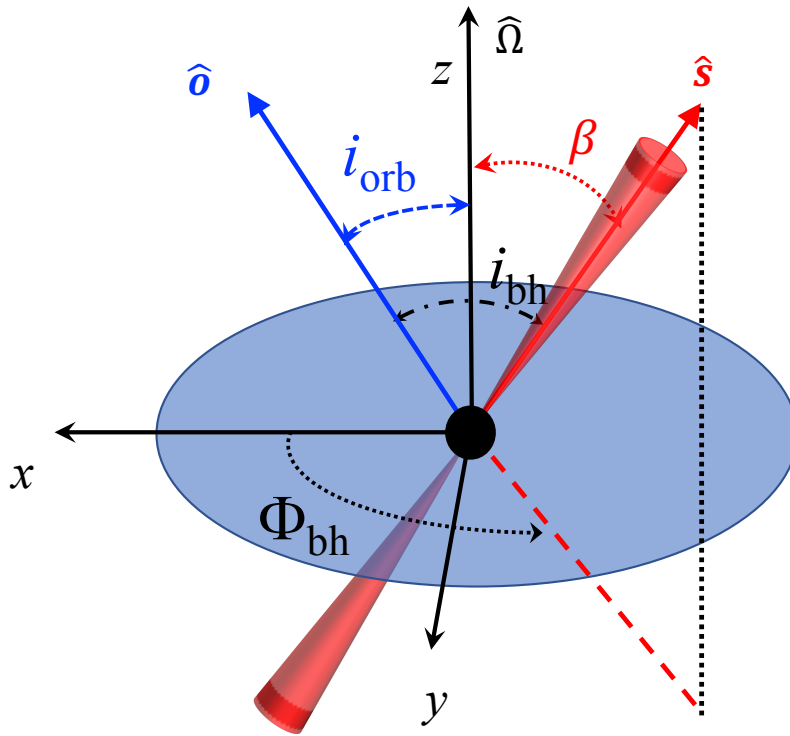


Figure S4: Geometry of the system. The orbital plane here coincides with the $x - y$ plane of the Cartesian system with the orbital axis being along the z -axis. The observer is situated in the $x - z$ plane at inclination angle i_{orb} as measured from the orbital axis. The black hole spin is directed at angle β from the z -axis at azimuthal angle Φ_{bh} as measured from the x -axis in the counter-clockwise direction in the $x - y$ plane as viewed from the top.

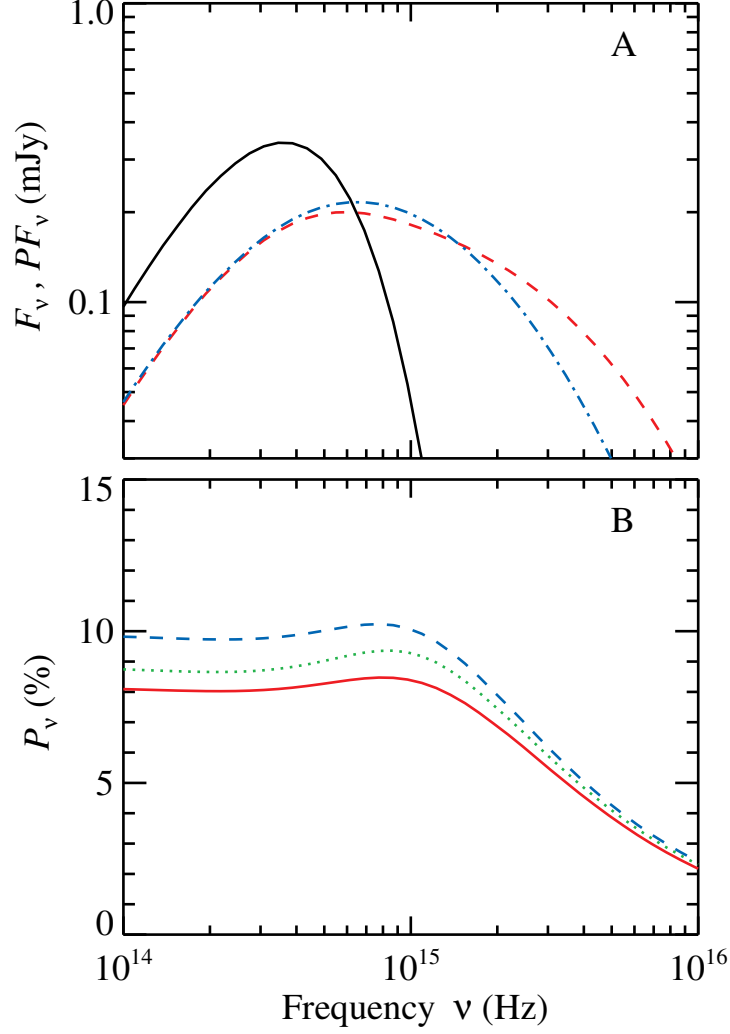


Figure S5: Polarization properties of ADAF model. (A) Flux from the spectral components: blackbody ($T_{\text{bb}} = 6200$ K, black solid line) and first Compton scattering of these photons by hot medium with $kT_e = 200$ keV and scale-height $\eta_{\text{crit}} = \cos \alpha_{\text{crit}} = 0.5$ (red dashed line), and spectrum of the polarized flux of the first scattering component (blue dot-dashed line) has been scaled up to match the low-energy part of the intensity spectrum (divided by the PD at low energies). Only results for inclination of $i_{\text{orb}} = 73^\circ$ are shown, as the dependence on the inclination in its allowed range is minor. (B) PD as a function of frequency is shown for different inclinations $i_{\text{orb}} = 81^\circ$ (blue dashed line), 73° (green dotted) and 66° (red solid). PD for energies below the peak of the scattered component is nearly frequency-independent.

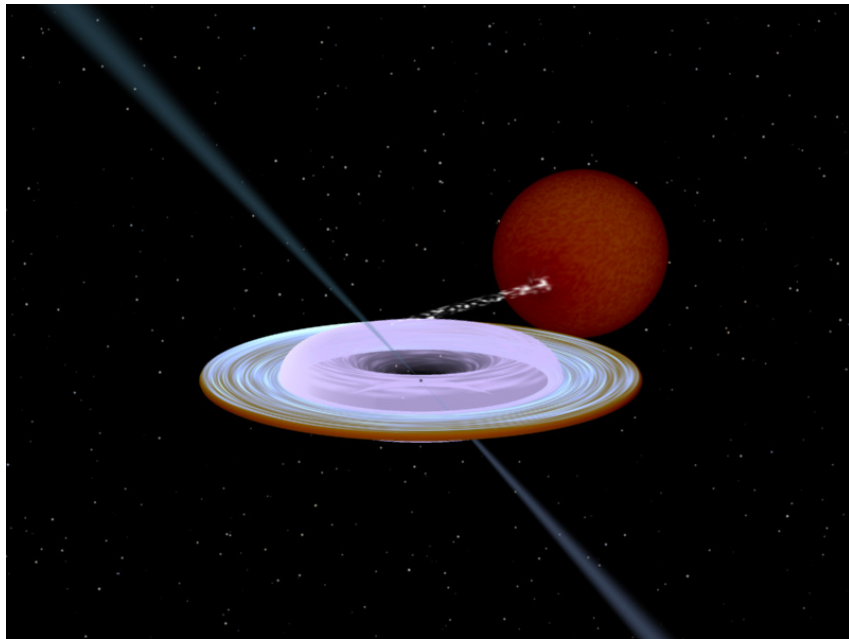


Figure S6: Illustration of the geometry. Artist impression of the black hole x-ray binary system MAXI J1820+070 with the companion star, the outer disk, central hot flow, and the jet. Image produced with Binsim (63).

Table S1: Intrinsic polarization of MAXI J1820+070. The intrinsic values of the PD and PA for observations of MAXI J1820+070 during the outburst with DIPol-2 (22, 23) and the quiescence with DIPol-UF at NOT. Errors are 1σ . The Stokes parameters for the interstellar polarization were subtracted from the observed Stokes parameters. The dates for observations in quiescence correspond to the middle of observing windows of a typical duration of one hour.

Date (MJD)	<i>B</i>		<i>V</i>		<i>R</i>	
	PD (%)	PA (deg)	PD (%)	PA (deg)	PD (%)	PA (deg)
Outburst						
58195–58222	0.28 ± 0.01	9.2 ± 1.0	0.36 ± 0.01	22.9 ± 1.0	0.30 ± 0.01	29.0 ± 0.9
58223–58234	0.34 ± 0.02	8.8 ± 1.4	0.51 ± 0.02	23.4 ± 1.4	0.53 ± 0.02	23.9 ± 1.1
58312–58344	0.16 ± 0.01	-15.8 ± 1.6	0.15 ± 0.01	13.4 ± 2.3	0.02 ± 0.01	39.1 ± 11.0
58406–58428	0.06 ± 0.04	-3.0 ± 15.4	0.13 ± 0.06	2.8 ± 12.4	0.09 ± 0.04	44.8 ± 12.5
Quiescence						
58686.93	3.86 ± 0.29	-23.8 ± 2.1	1.81 ± 0.24	-23.8 ± 3.8	0.70 ± 0.14	-24.1 ± 5.7
58688.01	2.35 ± 0.38	-25.9 ± 4.7	1.09 ± 0.25	8.0 ± 6.5	1.70 ± 0.10	-42.4 ± 1.7
58961.15	1.47 ± 0.28	-26.8 ± 5.4	0.52 ± 0.24	-4.2 ± 13.3	0.63 ± 0.19	8.5 ± 8.7
58964.16	4.31 ± 0.28	-18.5 ± 1.8	3.10 ± 0.29	-17.5 ± 2.7	1.05 ± 0.18	-2.0 ± 4.8
58965.11	2.81 ± 0.24	-23.5 ± 2.5	2.12 ± 0.21	-35.1 ± 2.9	0.84 ± 0.18	-26.3 ± 6.2
58967.12	4.53 ± 0.28	-24.1 ± 1.8	2.09 ± 0.39	-11.0 ± 5.3	1.09 ± 0.31	-27.0 ± 8.3
59050.94	4.58 ± 0.34	-15.3 ± 2.1	3.57 ± 0.31	-16.5 ± 2.5	1.54 ± 0.18	-14.5 ± 3.4
59050.98	5.03 ± 0.30	-11.0 ± 1.7	3.38 ± 0.34	-11.7 ± 2.9	1.62 ± 0.16	0.3 ± 2.9
59051.05	3.35 ± 0.26	-23.5 ± 2.2	2.04 ± 0.23	-17.1 ± 3.2	1.08 ± 0.18	-12.1 ± 4.9
59051.10	3.14 ± 0.30	-10.7 ± 2.7	1.95 ± 0.29	-4.8 ± 4.3	0.95 ± 0.16	5.6 ± 4.9
59051.92	4.08 ± 0.27	-18.1 ± 1.9	3.40 ± 0.25	-12.9 ± 2.1	1.39 ± 0.15	-18.0 ± 3.1
59051.97	4.67 ± 0.30	-16.5 ± 1.8	3.27 ± 0.30	-17.5 ± 2.6	1.96 ± 0.15	-17.9 ± 2.2
59052.03	4.83 ± 0.31	-16.7 ± 1.9	3.37 ± 0.24	-10.3 ± 2.1	1.68 ± 0.15	-20.0 ± 2.6
59052.09	3.78 ± 0.23	-21.5 ± 1.7	2.47 ± 0.22	-28.0 ± 2.5	1.06 ± 0.16	-12.4 ± 4.3
59052.92	4.14 ± 0.23	-24.2 ± 1.6	2.46 ± 0.23	-16.6 ± 2.7	1.21 ± 0.14	-18.4 ± 3.3
59052.98	3.30 ± 0.28	-20.5 ± 2.4	2.18 ± 0.23	-23.6 ± 3.0	1.18 ± 0.17	-14.0 ± 4.0
59053.92	4.02 ± 0.25	-12.8 ± 1.8	2.22 ± 0.26	-3.5 ± 3.4	1.24 ± 0.15	0.2 ± 3.4
59053.97	4.30 ± 0.27	-16.5 ± 1.8	3.18 ± 0.24	-10.4 ± 2.1	1.51 ± 0.15	-13.1 ± 2.9
Interstellar polarization						
58195–59054	0.81 ± 0.03	64.0 ± 1.1	0.71 ± 0.03	68.4 ± 1.2	0.60 ± 0.02	64.4 ± 0.8

Table S2: Log of observations with the Liverpool Telescope. The observed fluxes of MAXI J1820+070 and their errors in various filters.

Date (MJD)	Filter	Exposure (s)	Flux (mJy)	Date (MJD)	Filter	Exposure (s)	Flux (mJy)
59050.92075	<i>i</i>	100	0.2700±0.0014	59052.92842	<i>z</i>	100	0.3944±0.0033
59050.92213	<i>i</i>	100	0.2468±0.0015	59052.92980	<i>z</i>	100	0.4037±0.0033
59050.92350	<i>i</i>	100	0.2482±0.0015	59052.93193	<i>V</i>	200	0.1605±0.0011
59050.92505	<i>z</i>	100	0.3990±0.0028	59052.93463	<i>B</i>	200	0.0974±0.0007
59050.92642	<i>z</i>	100	0.4093±0.0029	59052.93637	<i>r</i>	40	0.3063±0.0018
59050.92780	<i>z</i>	100	0.3733±0.0029	59052.93705	<i>r</i>	40	0.2142±0.0018
59050.93052	<i>V</i>	300	0.1440±0.0009	59053.92120	<i>i</i>	100	0.3071±0.0017
59051.01279	<i>i</i>	100	0.3321±0.0014	59053.92257	<i>i</i>	100	0.3600±0.0018
59051.01417	<i>i</i>	100	0.3075±0.0014	59053.92395	<i>i</i>	100	0.3450±0.0018
59051.01554	<i>i</i>	100	0.3164±0.0014	59053.92550	<i>z</i>	100	0.3917±0.0033
59051.01709	<i>z</i>	100	0.4208±0.0027	59053.92687	<i>z</i>	100	0.3598±0.0033
59051.01846	<i>z</i>	100	0.5048±0.0028	59053.92825	<i>z</i>	100	0.3736±0.0034
59051.01984	<i>z</i>	100	0.4703±0.0027	59053.93038	<i>V</i>	200	0.1369±0.0011
59051.02254	<i>B</i>	300	0.1263±0.0005	59053.93308	<i>B</i>	200	0.0762±0.0007
59051.09342	<i>i</i>	100	0.3476±0.0016	59053.93482	<i>r</i>	40	0.2281±0.0019
59051.09479	<i>i</i>	100	0.3489±0.0016	59053.93550	<i>r</i>	40	0.2174±0.0019
59051.09617	<i>i</i>	100	0.3809±0.0015	59053.95474	<i>i</i>	100	0.2752±0.0016
59051.09771	<i>z</i>	100	0.4877±0.0032	59053.95612	<i>i</i>	100	0.2927±0.0016
59051.09909	<i>z</i>	100	0.4963±0.0033	59053.95750	<i>i</i>	100	0.2633±0.0017
59051.10047	<i>z</i>	100	0.4706±0.0033	59053.95904	<i>z</i>	100	0.3587±0.0032
59051.10168	<i>r</i>	40	0.2339±0.0019	59053.96042	<i>z</i>	100	0.3824±0.0030
59051.10236	<i>r</i>	40	0.2592±0.0018	59053.96180	<i>z</i>	100	0.4097±0.0033
59051.92206	<i>i</i>	100	0.3003±0.0015	59053.96393	<i>V</i>	200	0.1467±0.0010
59051.92343	<i>i</i>	100	0.2982±0.0015	59053.96663	<i>B</i>	200	0.0799±0.0007
59051.92481	<i>i</i>	100	0.2860±0.0015	59053.97116	<i>i</i>	100	0.3032±0.0042
59052.01060	<i>i</i>	100	0.2838±0.0016	59053.97254	<i>i</i>	100	0.3390±0.0016
59052.01197	<i>i</i>	100	0.2693±0.0015	59053.97391	<i>i</i>	100	0.3308±0.0016
59052.01335	<i>i</i>	100	0.2501±0.0016	59053.97546	<i>z</i>	100	0.4278±0.0032
59052.09336	<i>i</i>	100	0.2979±0.0015	59053.97684	<i>z</i>	100	0.4017±0.0032
59052.09474	<i>i</i>	100	0.2800±0.0016	59053.97821	<i>z</i>	100	0.4193±0.0031
59052.09611	<i>i</i>	100	0.2974±0.0015	59053.98035	<i>V</i>	200	0.1535±0.0010
59052.92275	<i>i</i>	100	0.3161±0.0017	59053.98305	<i>B</i>	200	0.0601±0.0007
59052.92412	<i>i</i>	100	0.3058±0.0016	59053.98479	<i>r</i>	40	0.2427±0.0017
59052.92550	<i>i</i>	100	0.3048±0.0017	59053.98546	<i>r</i>	40	0.2100±0.0017
59052.92705	<i>z</i>	100	0.3686±0.0034				

Table S3: Parameters of the spectral fit. Distance of 2.96 kpc and inclination $i_{\text{orb}} = 70^\circ$ are assumed.

Parameter	Value	Units
T_{in}	6200^{+1400}_{-900}	K
R_{in}	$(6.3^{+2.7}_{-1.9}) \times 10^{10}$	cm
T_{bb}	15500^{+2700}_{-1600}	K
R_{bb}	$(8.1^{+1.8}_{-2.2}) \times 10^9$	cm
T_*	4500	K
R_*	5×10^{10}	cm
P_{UV}	$0.062^{+0.026}_{-0.014}$	

Table S4: Geometrical parameters. Geometrical parameters for the 16 possible cases of relative orientation of the orbital and the black hole spins.

		$i_{\text{bh}} = i_{\text{jet}} = 63^\circ \pm 3^\circ$		$i_{\text{bh}} = 180^\circ - i_{\text{jet}} = 117^\circ \pm 3^\circ$	
		$\theta_{\text{bh}} = \theta_{\text{jet}} + 180^\circ = 205^\circ 1 \pm 1^\circ 4$		$\theta_{\text{bh}} = \theta_{\text{jet}} = 25^\circ 1 \pm 1^\circ 4$	
		$i_{\text{orb}} = 73^\circ \pm 6^\circ$	$i_{\text{orb}} = 107^\circ \pm 6^\circ$	$i_{\text{orb}} = 73^\circ \pm 6^\circ$	$i_{\text{orb}} = 107^\circ \pm 6^\circ$
Polarization parallel to the meridional plane					
$\theta_{\text{orb}} = \text{PA} = -18^\circ 8 \pm 0^\circ 5$	β (deg)	117.9 ± 4.3	138.4 ± 2.2	62.1 ± 4.3	41.6 ± 2.2
	Φ_{bh} (deg)	44.6 ± 3.3	69.6 ± 7.1	224.6 ± 3.3	249.6 ± 7.1
$\theta_{\text{orb}} = \text{PA} + 180^\circ$	β (deg)	41.6 ± 2.2	62.1 ± 4.3	138.4 ± 2.2	117.9 ± 4.3
	Φ_{bh} (deg)	290.3 ± 7.1	315.4 ± 3.3	110.4 ± 7.1	135.4 ± 3.3
Polarization perpendicular to the meridional plane					
$\theta_{\text{orb}} = \text{PA} + 90^\circ$	β (deg)	116.4 ± 4.2	136.4 ± 2.2	63.6 ± 4.2	43.6 ± 2.2
	Φ_{bh} (deg)	314.0 ± 3.3	290.3 ± 6.7	134.0 ± 3.3	110.3 ± 6.7
$\theta_{\text{orb}} = \text{PA} + 270^\circ$	β (deg)	43.6 ± 2.2	63.6 ± 4.2	136.4 ± 2.2	116.4 ± 4.2
	Φ_{bh} (deg)	69.7 ± 6.7	46.0 ± 3.3	249.7 ± 6.7	226.0 ± 3.3